TASK QUARTERLY 13 No 1–2, 155–181

MODELING THE CONTACT OF STIFF AND SOFT BODIES WITH A RIGID SUPPORT BY SHORT RANGE FORCE FIELDS

ALESSANDRO CONTENTO[1], ANGELO DI EGIDIO[1], JACEK DZIEDZIC[2] AND AMABILE TATONE[1]

[1]*Department of Structural, Hydraulic and Geotechnical Engineering, University of L'Aquila, P.le Pontieri 1, 67040 Monteluco di Roio (AQ), Italy*
conte@ing.univaq.it

[2]*Department of Technical Physics and Applied Mathematics, Gdansk University of Technology, Narutowicza 11/12, 80-233 Gdansk, Poland*

(Received 1 December 2008; revised manuscript received 12 January 2009)

Abstract: Body impact-contact dynamics is a classical subject in mechanics. Most of the papers on the subject are based on a kinematical or impulse-exchange approach. In this paper a different approach has been adopted. It consists in assigning a constitutive description for the contact forces between the boundaries of bodies which get close to each other. In particular, a field of short range forces has been used to model the interaction between an affine body and the planar surface of a fixed rigid support. These forces are able to describe the impact, friction and adhesion allowing the body to have complex motions which look rather realistic. By an affine body we mean a body which undergoes affine, or homogeneous, deformations. Depending on the material, such a body can show very different behavior, from a quite rigid motion to a motion characterized by very large deformations. A soft body is assumed to be made of a viscous incompressible Mooney-Rivlin material. Though a microscopic model of surface interaction could be used in a multiscale approach, the description provided here is macroscopic only.

Keywords: impact, contact, short range interaction, soft body dynamics

1. Introduction

Contact mechanics is one of the most important subjects in solid mechanics. It is usually characterized by inequalities describing unilateral constraints enforcing the physical impenetrability of bodies. The corresponding lack of tensile contact tractions is removed only when adhesion forces are added. Given the general equations for the contact problem, different solution schemes and computational methods can be used to simulate the behavior of bodies in contact and to compute displacement and stress fields. The first work on this subject is the article by Hertz [1], published in 1882, on the frictionless contact between two elastic bodies.

In the last century, contact mechanics has been the subject of several papers in which the formulation was based on an extension of Hertz's analysis to other shapes and constitutive laws. Specific engineering problems, concerning mainly tribology and indentation hardness have been analyzed both at macro and micro scales. Excellent reviews on contact problems and models can be found in [2] and [3]. Being quite a general modeling problem, the adhesive contact between spheres has been probably the most investigated one over a period of several decades [4–7]. A numerical analysis of this problem has been carried out in [8] where the Lennard-Jones potential is used to describe molecular interactions and also in [9–11]. In [12, 13] macroscopic laws describing the interactions between surfaces have been obtained starting from an analysis of molecular interactions using a method developed in [14].

There are several possible ways for classifying contact modeling. At a macro scale, models can be collected into two main groups. The bodies in the first group are assumed to be rigid [15–17] and the contact is modeled by using impulse-exchange methods [18–22]. In the second group, deformable joint layers are introduced and the contact problem is mainly defined through a variational inequality, based on the Signorini contact law. Basically, two methods have been employed to cope with constraints: the Lagrangian multiplier method [23, 24] and the penalty method [25, 26] (more details on both methods can be found in [27]). This group contains both continuum-based models [28] and models based on discretization techniques [29]. Some of them take into account thermoelastic contact phenomena [30].

Another distinction can be made between models with or without friction. A regularized Coulomb friction law is usually adopted. In earlier works with friction [31, 32] a monotonically increasing tangential force was introduced. Lately, generalizations have been proposed in [33] and [34].

At lower scales the Hertzian assumption of smoothness is difficult to apply because of the contact surface roughness. A model of friction that takes into account the role of asperities is presented in [35]. The first models of rough surfaces were considered in [36, 37], while a fractal description of the surface was introduced in contact problems in [38] and [39].

A model that takes into account the effect of the contact surface elastic deformation on the distribution of contact area is presented in [40].

The aim of this paper is to devise a contact model capable of describing the complex motions of a stiff or soft body interacting with a rigid flat support, while being characterized by a computational simplicity. The approach consists in assigning constitutive laws for the contact forces between the body boundary and the support surface which get close to each other, without resorting to inequalities and complex computational rules related to unilateral constraints. The contact interaction is modeled by four short range force fields of different kind: (i) a repulsive force field; (ii) an adhesive force field, both described by a Lennard-Jones-like potential; (iii) a damping force field, describing the impact dissipation and depending both on the normal velocity and on the distance; (iv) a frictional force field, depending both on the sliding velocity and on the distance.

The basic idea is to use interaction force laws, similar to those obtained in [8–14] through an analysis starting at the molecular interaction level, to characterize

macroscopic *surface* tractions. All of these force fields depend on the distance between the rigid body boundary and the rigid support surface. They decay very fast as the distance increases and grow to infinity as the body and the support get closer and closer. The body will never *touch* the support. Instead, the true *contact distance* will depend on the motion, although some characteristic values for the distance can be related to the constitutive properties of each of the contact force fields.

Though the friction force field used here does not implement a Coulomb like friction, our model turns out to be particularly suitable to describe the dynamical behavior of a rigid body interacting with a surface, where two different dissipation mechanisms are at work, as explained above.

The motions described by our model, being generated by a single set of equations, show a smooth transition from usually separated phases like bouncing, rocking, free flight, sliding, slide-rocking. Even though this smoothness can often be observed only at a short time scale.

In this regard, it is necessary to point out the crucial role played by the time integration algorithm because of the high accuracy required near the impact, when the contact forces reach the greatest intensity. This fact can be given a mechanical interpretation by observing that the impact, rebound and sliding are events which are usually observed on a macroscopic scale but whose underlying mechanisms are visible only on a microscopic scale. That is why, in order to simulate a realistic motion, it would be of paramount importance to identify the constitutive parameters through a microscopic analysis of the contact interactions. Nevertheless, we have found it appealing and instructive to perform several numerical simulations of both two-dimensional and three-dimensional motions, which we will show and discuss with the aim to illustrate how the motion can be characterized by some macroscopic constitutive parameters.

The simulations show both stiff and soft bodies in different shapes. A stiff body is modeled as a rigid body while a soft body is supposed to be made of a rubber-like material characterized by Mooney-Rivlin strain energy, incompressibility and a viscous dissipation.

2. Affine body

The motion of a body $\mathscr{B}$ is described at each time t by placement $\boldsymbol{p}$ defined on the *paragon shape* $\mathscr{D} \subset \mathscr{E}$:

$$\boldsymbol{p} : \mathscr{D} \times \mathscr{T} \to \mathscr{E}\,, \tag{1}$$

where $\mathscr{E}$ is a three-dimensional Euclidean space. An affine motion is characterized by the following representation:

$$\boldsymbol{p}(\boldsymbol{x},t) = \boldsymbol{p}_0(t) + \boldsymbol{F}(t)(\boldsymbol{x} - \boldsymbol{x}_0)\,, \tag{2}$$

where $\boldsymbol{x}_0$ is a given point of $\mathscr{D}$ and the *deformation gradient*:

$$\boldsymbol{F}(t) : \mathscr{V} \to \mathscr{V} \tag{3}$$

is a tensor, *i.e.* an endomorphism of the translation space of $\mathscr{E}$, such that $\det \boldsymbol{F} > 0$. An affine test velocity field $\boldsymbol{w}$ at time t has the representation:

$$\boldsymbol{w}(\boldsymbol{x}) = \boldsymbol{w}_0 + \boldsymbol{G}\boldsymbol{F}(t)(\boldsymbol{x} - \boldsymbol{x}_0)\,, \tag{4}$$

where $\boldsymbol{G}$ is the test velocity gradient tensor. By assuming, as *the balance principle*, that at any time t:

$$\int_{\mathscr{D}} \boldsymbol{b}(\boldsymbol{x},t)\cdot\boldsymbol{w}\,dV+\int_{\partial\mathscr{D}} \boldsymbol{q}(\boldsymbol{x},t)\cdot\boldsymbol{w}\,dA-\boldsymbol{S}(t)\cdot\boldsymbol{G}\boldsymbol{F}(t)\,\mathrm{vol}\mathscr{D}=0, \tag{5}$$

for any test velocity field $\boldsymbol{w}$, we get the following equations of motion:

$$\begin{aligned} &-m\ddot{\boldsymbol{p}}_0(t)-m\boldsymbol{g}+\boldsymbol{f}(t)=0,\\ &-\ddot{\boldsymbol{F}}(t)\boldsymbol{J}\boldsymbol{F}(t)^T+\big(\boldsymbol{M}(t)-\boldsymbol{S}(t)\,\mathrm{vol}(\mathscr{D})\big)\boldsymbol{F}(t)^T=0, \end{aligned} \tag{6}$$

where $\boldsymbol{S}$ is the Piola Kirchhoff stress, and the bulk density force $\boldsymbol{b}$ has been assumed to be composed of the inertial force and the gravity force densities:

$$\boldsymbol{b}(\boldsymbol{x},t):=-\rho(\ddot{\boldsymbol{p}}(\boldsymbol{x},t)+\boldsymbol{g}). \tag{7}$$

The Euler tensor has been denoted by $\boldsymbol{J}:=\int_{\mathscr{D}}\rho(\boldsymbol{x}-\boldsymbol{x}_0)\otimes(\boldsymbol{x}-\boldsymbol{x}_0)dV$, the total mass by $m:=\int_{\mathscr{D}}\rho dV$ and $\boldsymbol{x}_0$ has been chosen to be the center of mass of $\mathscr{D}$. The different contact force fields $\boldsymbol{q}_j$ on the boundary give rise to the total force:

$$\boldsymbol{f}(t):=\sum_j\int_{\partial\mathscr{D}}\boldsymbol{q}_j(\boldsymbol{x},t)dA \tag{8}$$

and to the moment:

$$\boldsymbol{M}(t):=\sum_j\int_{\partial\mathscr{D}}(\boldsymbol{x}-\boldsymbol{x}_0)\otimes\boldsymbol{q}_j(\boldsymbol{x},t)dA. \tag{9}$$

3. Stress and material response

The main properties of stress together with constitutive assumptions are summarized here. By the frame indifference principle:

$$\boldsymbol{S}\cdot\boldsymbol{W}\boldsymbol{F}=0\quad\forall\,\boldsymbol{W}\mid\mathrm{sym}\,\boldsymbol{W}=0\quad\Rightarrow\quad\mathrm{skw}\,\boldsymbol{S}\boldsymbol{F}^T=0. \tag{10}$$

When considering a soft body we assume it to be made of an incompressible Mooney-Rivlin material defined by the strain energy function:

$$\varphi(\boldsymbol{F}):=c_{10}(\imath_1(\boldsymbol{C})-3)+c_{01}(\imath_2(\boldsymbol{C})-3), \tag{11}$$

where c_{10} and c_{01} are elastic moduli and $\imath_1(\boldsymbol{C})$ and $\imath_2(\boldsymbol{C})$ are the principal invariants of the Cauchy-Green tensor $\boldsymbol{C}:=\boldsymbol{F}\boldsymbol{F}^T$, which can be given the expressions:

$$\imath_1(\boldsymbol{C}):=\mathrm{tr}\,(\boldsymbol{C})=\boldsymbol{F}\cdot\boldsymbol{F},\quad\imath_2(\boldsymbol{C}):=\boldsymbol{F}^\star\cdot\boldsymbol{F}^\star, \tag{12}$$

where $\boldsymbol{F}^\star:=\boldsymbol{F}^{-T}\det\boldsymbol{F}$ is the cofactor of $\boldsymbol{F}$.

The way in which the stress depends on the motion can be characterized by a decomposition of the stress into three parts:

$$\boldsymbol{S}\boldsymbol{F}^T=\widehat{\boldsymbol{S}}(\boldsymbol{F})\boldsymbol{F}^T-\pi\boldsymbol{I}+\mu\,\mathrm{sym}(\dot\theta\boldsymbol{F}^{-1}). \tag{13}$$

Because of the incompressibility constraint $\det\boldsymbol{F}=1$ the velocity fields turn out to be isochoric, *i.e.* such that:

$$\mathrm{tr}\,\dot\theta\boldsymbol{F}^{-1}=0.$$

The condition for the *reactive* part $\boldsymbol{S}_r$ of the stress to spend null power on any isochoric test velocity field:

$$\boldsymbol{S}_r\cdot\boldsymbol{G}\boldsymbol{F}=0,\quad\mathrm{tr}\,\boldsymbol{G}=0,$$

implies that $\boldsymbol{S}_r\boldsymbol{F}^T$ is a spherical tensor which can be denoted by $-\pi\boldsymbol{I}$.

The *energetic* part $\widehat{\boldsymbol{S}}(\boldsymbol{F})$ is related to the strain energy function by the condition that in any motion:

$$\widehat{\boldsymbol{S}}(\boldsymbol{F})\cdot\dot{\theta}=d\varphi(\boldsymbol{F})/dt, \tag{14}$$

which is equivalent to assume the following response function:

$$\widehat{\boldsymbol{S}}(\boldsymbol{F})\,\boldsymbol{F}^T=2(c_{10}\boldsymbol{F}\,\boldsymbol{F}^T-c_{01}\boldsymbol{F}^{-T}\boldsymbol{F}^{-1}). \tag{15}$$

As the spherical part of this expression would be indistinguishable from the reactive part of the stress, which is also spherical, we can restrict the response function (15) to its deviatoric part.

Further, we assume that there is a *dissipative* part of the stress $\boldsymbol{S}_+$ such that:

$$\boldsymbol{S}_+\boldsymbol{F}^T=\mu\,\mathrm{sym}\,(\dot{\theta}\boldsymbol{F}^{-1}).$$

The *dissipation principle*, stating that in any isochoric motion:

$$\boldsymbol{S}\cdot\dot{\theta}-d\varphi(\boldsymbol{F})/dt\geq 0 \tag{16}$$

turns out to be satisfied, after replacing (13), by the only condition $\mu\geq 0$.

4. Contact force constitutive laws

Denoting by $\boldsymbol{o}$ any place on the flat surface $\mathscr{S}$ of the rigid support and by $\boldsymbol{n}$ the exterior unit normal vector to that surface, let us define the distance of the point $\boldsymbol{x}$ on $\partial\mathscr{D}$ from the flat surface $\mathscr{S}$ at time t (Figure 1):

$$d(\boldsymbol{x},t):=(\boldsymbol{p}(\boldsymbol{x},t)-\boldsymbol{o})\cdot\boldsymbol{n}, \tag{17}$$

where $\boldsymbol{p}(\boldsymbol{x},t)$ is the position occupied by $\boldsymbol{x}$ at time t. The distance of the body from the surface $\mathscr{S}$ is defined as the minimum value of $d(\boldsymbol{x},t)$ over the boundary $\partial\mathscr{D}$.

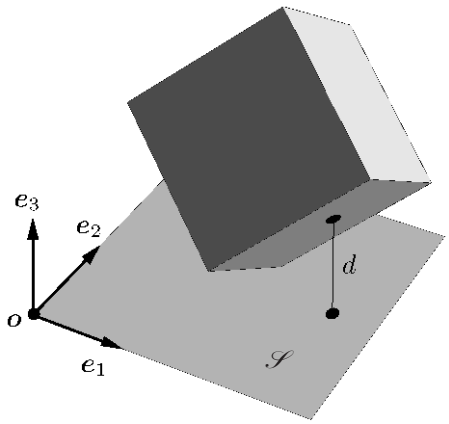

Figure 1. Body interaction with a rigid flat support

Due to large deformations that a soft body can undergo, when defining tractions per unit area of $\partial\mathscr{D}$ we have to take into account the area change factor:

$$k(\boldsymbol{x},t):=|\boldsymbol{F}^{\star}(\boldsymbol{x},t)\boldsymbol{m}(\boldsymbol{x},t)|, \tag{18}$$

where $\boldsymbol{m}$ is the unit normal to $\partial\mathscr{D}$. The *repulsive* traction field is assumed to be described by the following constitutive law:

$$\boldsymbol{q}_r(\boldsymbol{x},t)=k(\boldsymbol{x},t)\,\alpha_r\,d(\boldsymbol{x},t)^{-\nu_r}\,\boldsymbol{n}, \tag{19}$$

where the coefficient α_r is a positive real number and the exponent ν_r is a positive integer number. A value for α_r can be obtained by requiring that the repulsive forces balance the gravity forces when the body stays at rest at an equilibrium distance d_0 from a horizontal surface. In other words, α_r is determined by choosing a characteristic distance d_0. The impact dissipation can be described by the following *damping* traction on $\partial\mathscr{D}$:

$$\boldsymbol{q}_d(\boldsymbol{x},t) = -k(\boldsymbol{x},t)\,\beta_d\, d(\boldsymbol{x},t)^{-\nu_d}\,(\boldsymbol{n}\otimes\boldsymbol{n})\,\dot{\theta}(\boldsymbol{x},t), \tag{20}$$

where the damping factor β_d is a positive real number and ν_d a positive integer number. The tensor $(\boldsymbol{n}\otimes\boldsymbol{n})$ is the projector onto the direction orthogonal to $\mathscr{S}$. The *frictional* traction field is given the constitutive law:

$$\boldsymbol{q}_f(\boldsymbol{x},t) = -k(\boldsymbol{x},t)\,\beta_f\, d(\boldsymbol{x},t)^{-\nu_f}\,(\boldsymbol{I}-\boldsymbol{n}\otimes\boldsymbol{n})\,\dot{\theta}(\boldsymbol{x},t), \tag{21}$$

where the friction coefficient β_f is a positive real number and ν_f is a positive integer number. Differently from the previous traction fields, both normal to the surface $\mathscr{S}$, the frictional traction field is tangent to the surface $\mathscr{S}$.

In some simulations an adhesive force will be introduced and given the following law:

$$\boldsymbol{q}_a(\boldsymbol{x},t) = -k(\boldsymbol{x},t)\,\beta_a\left(d(\boldsymbol{x},t)^{-\nu_{aa}} - d(\boldsymbol{x},t)^{-\nu_{ar}}\right)\boldsymbol{n}, \tag{22}$$

where the coefficient β_a is a positive real number and ν_{aa} and ν_{ar} are positive integer numbers such that $\nu_{ar} < \nu_r$ and $\nu_{aa} = \nu_{ar}/2$. In Figure 2 repulsive and adhesive forces are compared. In order to illustrate the role of the parameters on which the contact tractions depend, it is worth making some remarks. All of the traction fields given by Equations (19)–(22) depend on the exponential function $d^{-\nu}$. It is interesting to observe how the spatial distribution of this function changes by varying the value of some parameters.

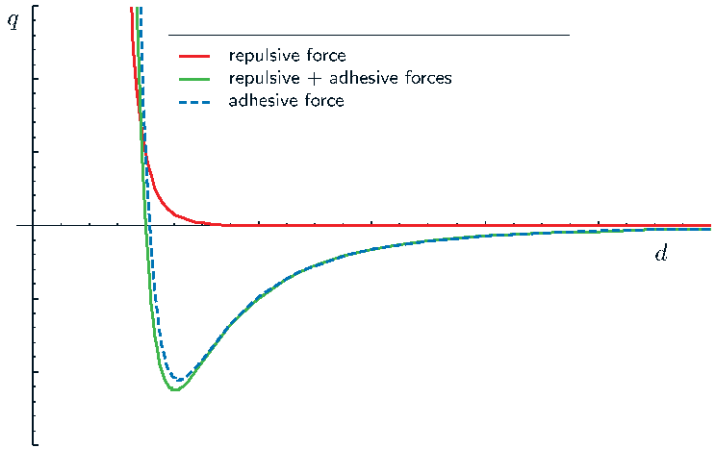

Figure 2. Comparison of repulsive and adhesive forces: $\nu_r = 8$, $\nu_{aa} = 3$, $\nu_{ar} = 6$

Figures 3a–c show how rapidly the graph of such an exponential function along the boundary changes when rotating a body in the shape of a cube around an edge. The same values for both d_0 and ν have been used for all graphs in Figure 3. When the lower face of the body is parallel to plane $\mathscr{S}$ (Figure 3a), the graph is flat; as soon

as the body rotates by a very small angle ($\theta = \pi/100$, Figure 3b) the graph rapidly decreases to zero from a maximum value attained at point P. Finally, when the body is in an unstable equilibrium configuration ($\theta = \pi/4$, Figure 3c) the graph becomes very sharp.

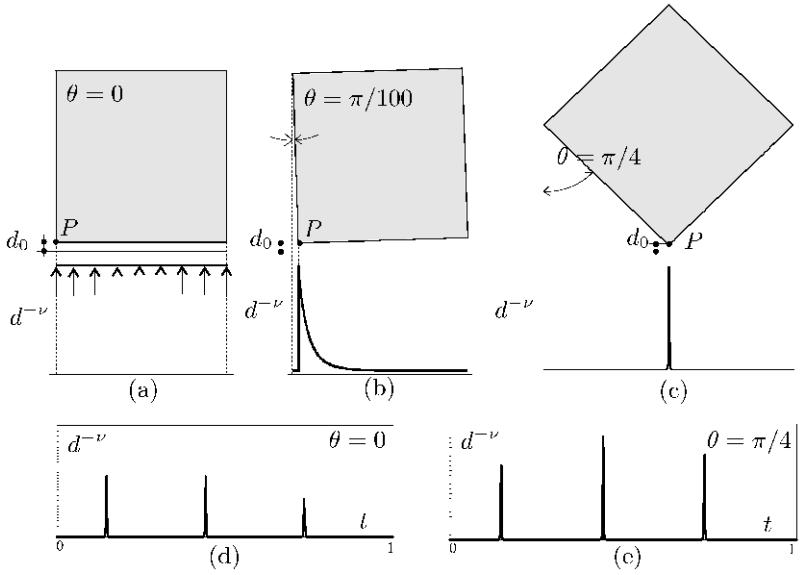

Figure 3. Spatial distribution and time evolution of the exponential function $d^{-\nu}$: (a) spatial distribution with the lower face parallel to the support surface; (b) spatial distribution when the body is rotated by $\theta = \pi/100$ about the left lower edge; (c) when the body is rotated by $\theta = \pi/4$; (d) time evolution at the corner P for $\theta = 0$; (e) time evolution at P for $\theta = \pi/4$ ($\nu = 6$, $d_0 = 0.01$)

Figures 3d–e show the time evolutions of the exponential function at point P, when the body bounces vertically starting from two different initial conditions: $\theta = 0$ (Figure 3d) and $\theta = \pi/2$ (Figure 3e). The real challenges that the numerical algorithm has to face when integrating the equations of motion (6) are to cope with such high unevenness of the tractions on the body boundary and with such a high variability in time.

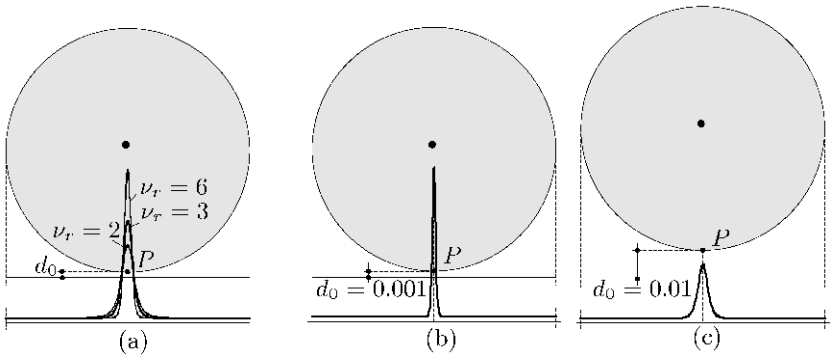

Figure 4. Spatial distribution of the repulsive forces: (a) for several values of the exponent ν_r and $d_0 = 0.01$; (b) $\nu_r = 3$, $d_0 = 0.001$; (c) $\nu_r = 3$, $d_0 = 0.01$

Figure 4 shows the spatial distribution of the repulsive forces (19), related to a plane motion of a circular cylinder. Graphs in Figure 4 have been obtained by fixing the characteristic distance d_0 and then computing the value for α_r that makes the total force f balance the weight of the body. As shown in Figure 4a the higher the value of the exponent ν_r, the sharper the repulsive force distribution. Something similar happens when, for a fixed exponent value ($\nu_r = 3$), the distance d_0 is changed (Figures 4b–c): the smaller the value of d_0, the sharper the repulsive force distribution. To summarize these results we can say that, for a fixed value of the total boundary traction f, either increasing the exponent ν_r or decreasing the distance d_0 make the traction distribution sharper.

In the following sections some selected simulations will be discussed. The positions will be described in general using coordinates in a Cartesian coordinate system, whose origin belongs to the support surface, as in Figure 1: coordinates x, y and z correspond to the basis vectors $\boldsymbol{e}_1$, $\boldsymbol{e}_2$, and $\boldsymbol{e}_3$, respectively. The support surface will be orthogonal to one of the three basis vectors, depending on the problem. The gravity force will be vertical and downward in all of the figures. By plane motion we mean a motion where the z coordinate of the position of any point of the body does not change with time.

5. Impact frequencies and damping

Some simple simulations have been performed in order to characterize the system's behavior and to understand the role of several parameters in the dynamical response. A rigid block in the shape of a cube is set to motion by two types of initial conditions: (i) an initial vertical shift v_0 from an equilibrium configuration or (ii) both an initial vertical shift v_0 and an initial rotation θ_0.

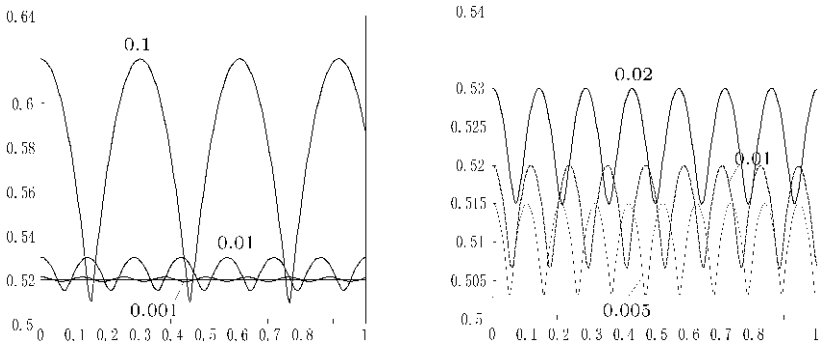

(a) (b)

Figure 5. (a) distance of the center from the support for several initial conditions ($d_0 = 0.02\,\mathrm{m}$, $\nu_r = 5$); (b) distance of the center from the support for several values of d_0 ($v_0 = 0.01\,\mathrm{m}$, $\nu_r = 5$)

Just in these first simulations, it is only repulsive and damping force fields that are supposed to exist and to be applied at the bottom face of the cube only. Further, the damping force is characterized by $\nu_d = 0$ (linear viscous damping). The motion is assumed to lie on a vertical plane. Due to the absence of friction the motion can be described by the vertical displacement $v(t)$ and the rotation amplitude $\theta(t)$.

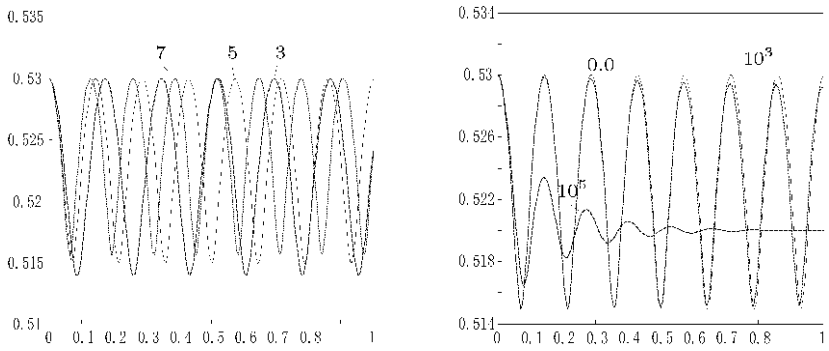

(a) (b)

Figure 6. (a) distance of the center from the support for several values of the exponent ν_r; ($d_0 = 0.02\,\mathrm{m}$, $v_0 = 0.01\,\mathrm{m}$); (b) distance of the center from the support for several values of the damping coefficient β_d; ($d_0 = 0.02\,\mathrm{m}$, $v_0 = 0.01\,\mathrm{m}$, $\nu_r = 5$)

First a simple vertical motion (bouncing) is triggered by an initial condition with $\theta = 0$. The equilibrium distance d_0, the initial upward vertical shift v_0 and the exponent ν_r of the constitutive law for the repulsive forces are varied in order to analyze how they affect the motion. The results show that the amplitude of the bouncing motion decreases as the initial shift v_0 decreases while the frequency decreases as the initial shift increases. The rigid block for a vanishing initial shift stays still in a stable equilibrium configuration (Figure 5a). It can be observed that the main consequence of lowering the equilibrium distance d_0 is a shift of the response. However, other minor effects can be noticed. Since the value of d_0 also affects the value of the force, as d_0 gets smaller the oscillation amplitude decreases while the frequency increases (Figure 5b). A variation of the exponent in the contact force constitutive law is reflected in a change of the motion frequency. In particular when the exponent is increased then the motion shows an increase in the frequency. An increase in the exponent slightly affects also the lowest position reached by the cube center (Figure 6a). The dissipative traction effect is analyzed by varying the viscosity coefficient. High values of the coefficient β_d are needed in order to observe a strong dissipative behavior.

Another interesting effect of this kind of dissipation is a decrease in the bouncing frequency during the motion (Figure 6b). Finally it is worth noting that this kind of a contact model makes it possible to observe a known relation between the oscillation amplitude and the motion frequency : the smaller the amplitudes of the displacement the higher the frequency, and vice versa.

When both the vertical shift and the rotation are given as initial conditions, the system exhibits richer dynamics. In Figure 7 the classical dynamical behavior of a system in which two frequencies are close to each other is clearly shown. One of these frequencies is associated with the vertical motion, while the other refers to the rocking motion, as can be noticed during the first quarter of the time-histories of the position of the center of mass (Figure 7a) and of the rotation (Figure 7b).

The viscous damping regularizes the system's behavior since the vertical motion associated with the frequency decreases faster than the frequency associated with the rocking. Figure 8 shows the position of the center of mass for several values

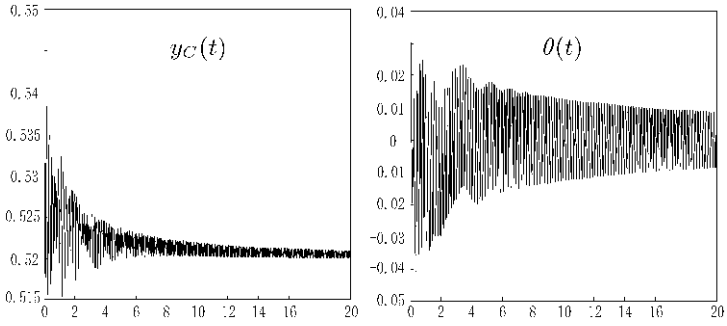

(a) (b)

Figure 7. (a) the distance of the center from the support; (b) rotation amplitude ($d_0 = 0.02\,\mathrm{m}$, $v_0 = 0.005\,\mathrm{m}$, $\theta_0 = 0.01\pi$, $\beta_d = 10^4\,\mathrm{Ns/m^2}$, $\nu_r = 5$)

of the initial rotation amplitude. It should be noticed that for a very small initial rotation (Figure 8a) the system seems to exhibit only the frequency related to the vertical motion since the rotation amplitude is very small. By increasing the initial rotation amplitude the system exhibits dynamics that reveals the existence of two close frequencies (Figures 8b–c). When the initial rotation amplitude is increased, the oscillation amplitude increases as well, and, as a direct consequence, all the frequencies decrease. Interesting behavior is exhibited when the contact forces exponent is varied. As already noticed, when ν_r is increased the frequency of the vertical motion increases, as well. The same happens to the rocking frequency, but the variation of the two frequencies follows different laws, when the exponent ν_r is changed. This fact explains the results shown in Figure 9. In Figure 9b the viscous damping seems to have a smaller effect than in Figure 9a and in Figure 9c. This situation can occur since the two frequencies for $\nu_r = 5$ strongly interact with each other because of an internal resonance condition, which does not exist for the other two values of ν_r.

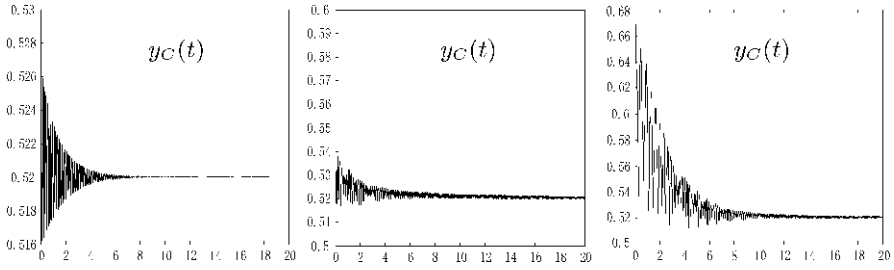

(a) (b) (c)

Figure 8. Distance of the center from the support for several initial values of the rotation amplitude: (a) $\theta_0 = 0.001\pi$, (b) $\theta_0 = 0.01\pi$, (c) $\theta_0 = 0.1\pi$ ($d_0 = 0.02\,\mathrm{m}$, $v_0 = 0.005\,\mathrm{m}$, $\beta_d = 10^4\,\mathrm{Ns/m^2}$, $\nu_r = 5$)

Quite a different motion can be obtained, as shown in Figure 10, in a simulation starting from a configuration close to the unstable equilibrium configuration where the cube lies on an edge. To this end, the impact and damping contact force fields have been extended to two adjacent faces (bottom face and left face) and the damping force exponent has been set to $\alpha_r = 2$, modeling in this way a higher dissipation near the

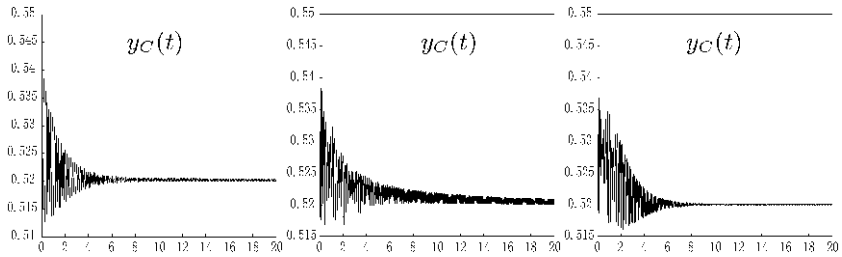

Figure 9. Distance of the center from the support for several values of the exponent: (a) $\nu_r = 3$, (b) $\nu_r = 5$, (c) $\nu_r = 7$ ($d_0 = 0.02\,\mathrm{m}$, $v_0 = 0.005\,\mathrm{m}$, $\theta_0 = 0.01\pi$, $\beta_d = 10^4\,\mathrm{Ns/m^2}$)

impact. It can be noticed in Figure 10 how the solution remains close to an unstable solution for a while and then it gets away from it. The time evolution of the left edge position reveals the existence of two frequencies of which one is related to the vertical motion and the other to the rocking motion. The phase portrait (Figure 10b) of the displacement versus the velocity of the left edge shows the transition from an unstable to a new stable equilibrium configuration. Finally it is worth noticing that small changes of displacement correspond to large changes of velocity near the impact.

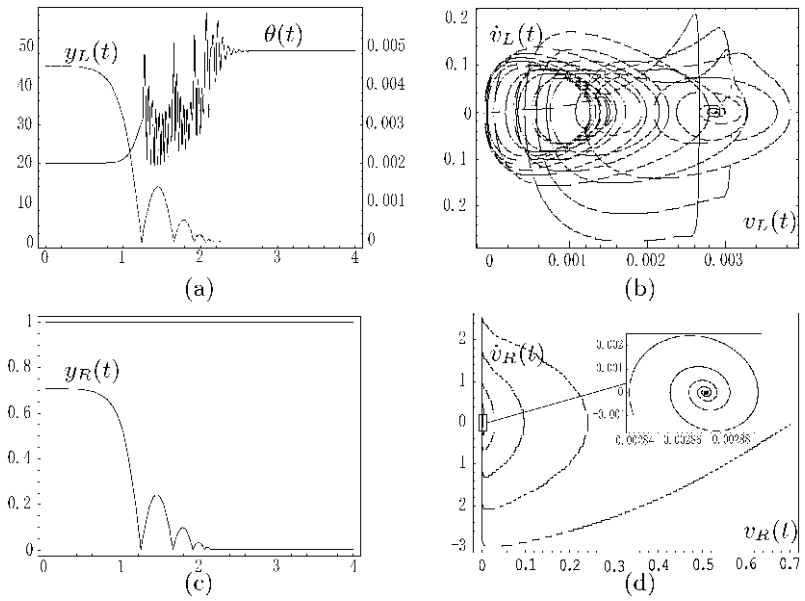

Figure 10. Two face contact model: (a) rotation amplitude and distance of the lower left edge from the support; (b) phase portrait of the lower left edge; (c) distance of the lower right edge from the support; (d) phase portrait of the lower right edge; ($d_0 = 0.02\,\mathrm{m}$, $v_0 = 0$, $\theta_0 = \pi/4$, $\nu_r = 8$, $\rho = 10^3\,\mathrm{kg/m^2}$, $\nu_d = 2$, $\beta_d = 1$)

6. Numerical simulations of 2D rigid motions

In order to asses the ability of the model to reproduce realistic behavior, several numerical simulations have been performed using different constitutive parameters

and starting from different initial conditions. The whole boundary of the body is supposed to be able to interact with the support surface according to the contact traction laws defined in Section 4, with uniform values of the coefficients α_r, β_d, β_f, β_a.

6.1. Sliding, bouncing and rocking

The numerical computation scheme can be briefly described as follows: the main procedure consists in the numerical integration of the equations of motion (6) starting from given initial conditions; at a lower level, for each time step, the main task consists in computing the integrals (8) and (9) over the boundary $\partial\mathscr{D}$. The whole procedure has been implemented in *Mathematica*®, which has also been used to derive the general expressions for each of the traction fields in Section 4, starting from the motion description (2) and making use of (5).

Figure 11 shows the plane motion of a rigid body in the shape of a cube starting from a slightly perturbed unstable equilibrium configuration. The left column, Figures 11a–d, refers to a contact without friction, while the right column, Figures 11e–h, refers to a contact with friction. The graphs show the time evolution of the distances $y_L(t)$ and $y_R(t)$ of the L and R edges from the support, together with the time evolution of the rotation amplitude $\theta(t)$. Both the initial configurations (gray) and the limit configurations (dashed) can be seen at the top of the figure. Looking at the left column (Figures 11b–c; frictionless contact) we can see how the edge L changes only slightly its distance from the support, while the edge R falls down in a clockwise rotation of the body (Figure 11d) until it starts bouncing. Both L and R edges reach, in a sufficiently long time span, the same distance from the support, slightly greater than the initial distance of the body because the body ends up lying on a flat face instead of an edge. This fact, together with the small oscillations exhibited by the L edge in the transition (Figure 11b), reveals the absence of a real contact surface. Indeed, the short range force fields depend on the distance between the rigid body and a conventional invisible barrier. When frictional forces are added, the system exhibits richer dynamics. As can be seen from the bouncing of both edges L and R (Figures 11f–g), the rigid motion resembles a rocking motion until it fades out. In the frictionless case (Figure 11a) the trajectory of the rigid body center turns out to be vertical. This means that while the body rotates, the edge L slides leftward. Instead, if the friction coefficient is large enough, the edge L does not slide any more, though it bounces for a while (Figures 11e–g), thus making the trajectory of the center very different, and even longer from the previous case. These differences could be related to the time interval separating the *impact times* t_k and t'_k (Figures 11c–g).

6.2. Rolling and bouncing

Figure 12 shows the plane motion of a rigid body in the shape of a circular cylinder. The left column, Figures 12b–d, refers to a contact without friction, while the right column, Figures 12e–g, refers to a contact with friction. Figures 12b–e and Figures 12c–f show the time evolution of the vertical and horizontal coordinates of the center $y_C(t)$ $x_C(t)$; Figures 12d–g show the time evolution of the angular velocity. The trajectory of the center drawn in the top panel, Figure 12a, has been rescaled to make the bouncing more visible. Although friction does not affect the time evolution of the

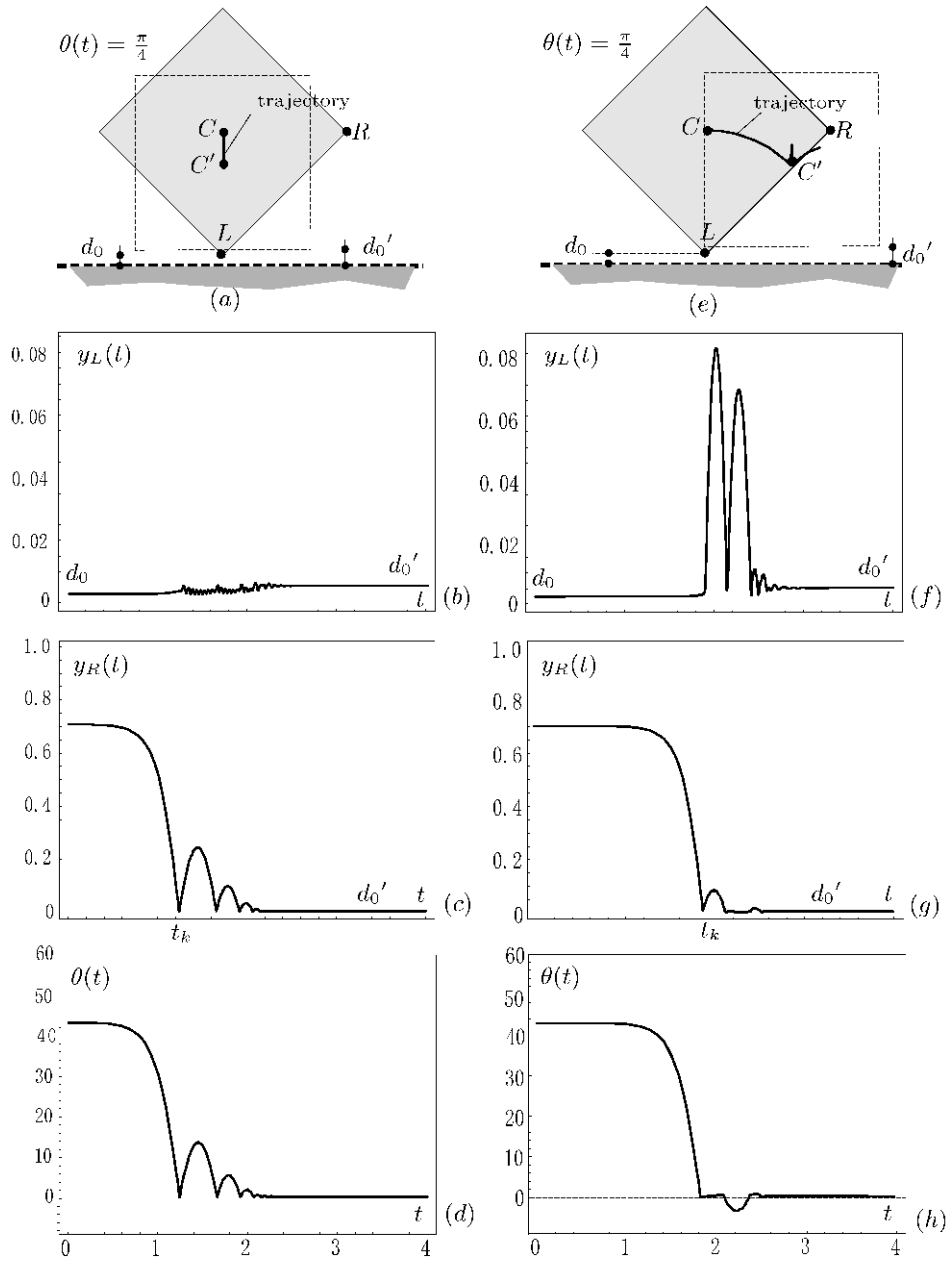

Figure 11. Plane motion of a rigid body in the shape of a cube: left column – contact without friction ($d_0 = 0.02\,\mathrm{m}$, $v_0 = 0$, $\theta_0 = 0.99\pi/4$, $\nu_r = 8$, $\rho = 10^3\,\mathrm{kg/m^2}$, $\nu_d = 0$, $\beta_d = 1$, $\beta_f = 0$); right column – contact with friction ($d_0 = 0.02\,\mathrm{m}$, $v_0 = 0$, $\theta_0 = 0.99\pi/4$, $\nu_r = 8$, $\rho = 10^3\,\mathrm{kg/m^3}$, $\nu_d = 0$, $\beta_d = 1$, $\beta_f = 100$, $\nu_f = 2$); (a)–(e) body initial and final configurations and trajectory of the center; (b)–(f) L edge distance from the support; (c)–(g) R edge distance from the support; (d)–(h) rotation amplitude

distance of the center from the support (the vertical motion of the body), as can be seen comparing Figure 12b and Figure 12e, it makes the motion quite different: at the first impact the angular velocity rises suddenly (Figure 12g), as a consequence of the

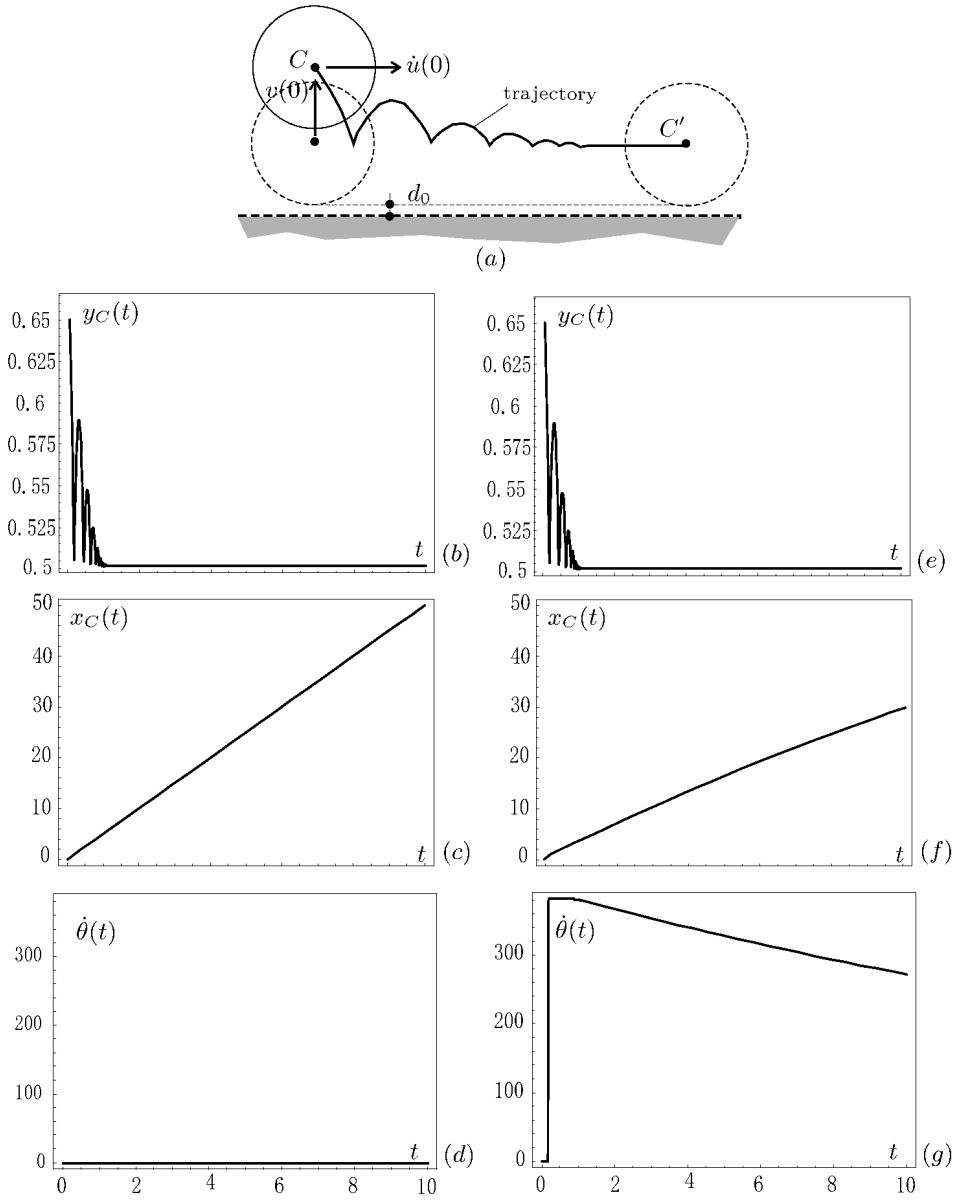

Figure 12. Plane motion of a rigid circular cylinder: left column – contact without friction ($d_0 = 0.02\,\mathrm{m}$, $v_0 = 0.15\,\mathrm{m}$, $\dot{\theta}_0 = 5\,\mathrm{m/s}$, $\nu_r = 8$, $\rho = 10^3\,\mathrm{kg/m^2}$, $\nu_d = 4$, $\beta_d = 10^{-5}$, $\beta_f = 0$); right column – contact with friction ($d_0 = 0.02\,\mathrm{m}$, $v_0 = 0.15\,\mathrm{m}$, $\dot{\theta}_0 = 5\,\mathrm{m/s}$, $\nu_r = 8$, $\rho = 10^3\,\mathrm{kg/m^2}$, $\nu_d = 4$, $\beta_d = 10^{-5}$, $\beta_f = 10^3$, $\nu_f = 6$)

initial value of the horizontal velocity. This means that the friction makes the cylinder roll while lowers at the same time the horizontal velocity (compare Figure 12f and Figure 12c). Finally, it is worth noting how the angular velocity decreases after the bouncing has faded out. This is a consequence of the damping forces (20) acting on the points close to the contact, whose vertical velocity is different from zero because of the rolling.

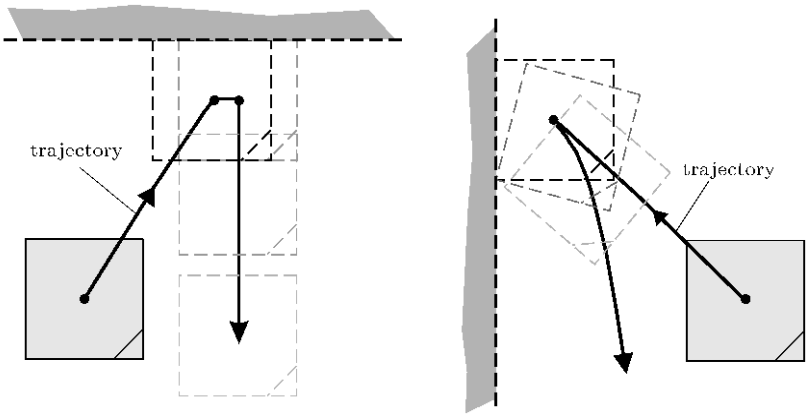

Figure 13. Effect of the adhesive forces: (a) adhesion to a ceiling; (b) adhesion to a vertical wall ($d_0 = 0.002\,\mathrm{m}$, $\nu_r = 8$, $\nu_a r = 6$, $\nu_a a = 3$, $\nu_d = 2$, $\nu_f = 6$, $\beta_a = \beta_d = 1$, $\beta_f = 10^5$)

6.3. Adhesion and detachment

Figure 13 shows the outcome of simulations where adhesive contact forces (22) have been added. To better understand the influence of adhesive forces these simulations consist in computing the motion generated by throwing the body against either a horizontal support (like a ceiling, Figure 13a) or a vertical support (like a wall, Figure 13b), in order not to confuse the adhesive forces with the gravity force. The given initial velocity allows the body to reach the support without bouncing back. Once the body has got stuck to the support, the mass density of the body is increased gradually as a trick to make the bond brake. And that is exactly what happens: the body detaches from the support and falls down.

The role of the friction is very different in the two simulations. While in case (a) the friction just slows down the body until it stops sliding on the ceiling, in case (b) the friction prevents the body from sliding down the wall until detachment. The trajectory of the body center and a few frames help to understand the motion.

6.4. Rocking on a sloping plane

Figures 14–16 show the plane motion of a rigid body over a sloping support ($\theta_s = \pm\pi/20$). An angular velocity $\dot{\theta}(0)$ is assigned as an initial condition to the body rotated by $\theta(0) = \pi/4$ from a configuration with a face lying on the support (Figure 14a). The time evolution of the distance of the L and R edges from the support (Figure 14b), together with the distance of the center C from the support (Figure 14c), shows the complexity of the motion. By the evolution of the rotation amplitude $\theta(t)$ (Figure 14c) it can be realized that the body performs many complete rotations until it stops.

The sloping plane better highlights the effects of friction. The motion in Figure 15 starts from the same initial conditions as the motion in Figure 14, but a lower friction coefficient β_f makes the two trajectories quite different.

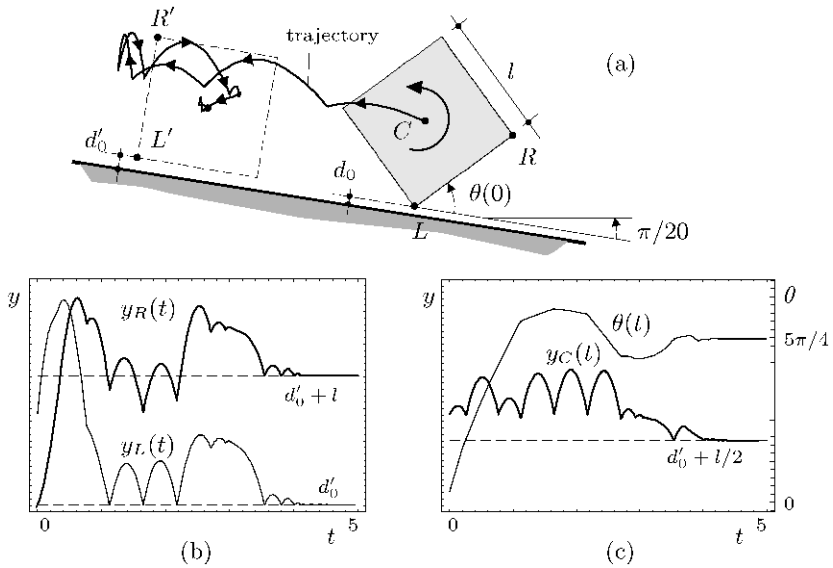

Figure 14. Motion on a sloping plane: (a) body shapes and trajectory of the center; (b) time-histories the L corner and the R corner distance from the support; (c) time-histories of the distance of the center from the support and of the rotation amplitude θ ($d_0 = 0.02\,\mathrm{m}$, $\dot\theta(0) = 20\,\mathrm{rad/s}$, $\nu_r = 8$, $\nu_d = \nu_f = 2$, $\beta_d = 1$, $\beta_f = 10^3$, $\rho = 10^3\,\mathrm{kg/m^2}$)

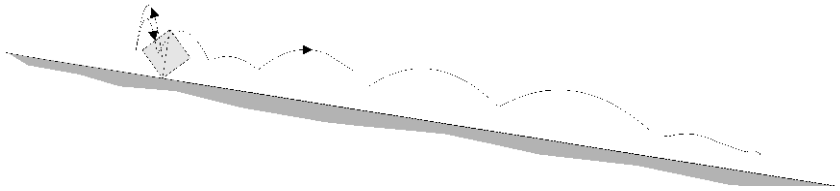

Figure 15. Motion on a sloping plane ($d_0 = 0.02\,\mathrm{m}$, $\theta_0 = \frac{\pi}{4}$, $\rho = 10^3\,\mathrm{kg/m^2}$, $\nu_r = 8$, $\nu_d = 2$, $\nu_f = 2$, $\beta_d = 1$, $\beta_f = 10$, $\theta_s = \frac{\pi}{20}$, $\dot\theta_0 = 20\,\mathrm{s^{-1}}$)

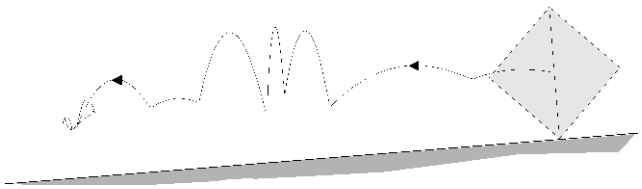

Figure 16. Motion on a sloping plane ($d_0 = 0.02\,\mathrm{m}$, $\theta_0 = \frac{\pi}{4}$, $\rho = 10^3\,\mathrm{kg/m^2}$, $\nu_r = 8$, $\nu_d = 2$, $\nu_f = 2$, $\beta_d = 1$, $\beta_f = 100$, $\theta_s = -\frac{\pi}{20}$, $\dot\theta_0 = 20\,\mathrm{s^{-1}}$)

7. Numerical simulations of 3D rigid motions

7.1. Spinning and bouncing

Several numerical simulations have been done to check the ability of the model to reproduce realistic behavior also in a 3D motion. Figures 17–20 describe the trajectories of a rigid body in the shape of a cube starting from an (unstable) equilibrium configuration where the body is placed on a corner V over a horizontal support, while the opposite corner stays on the vertical line n passing through the

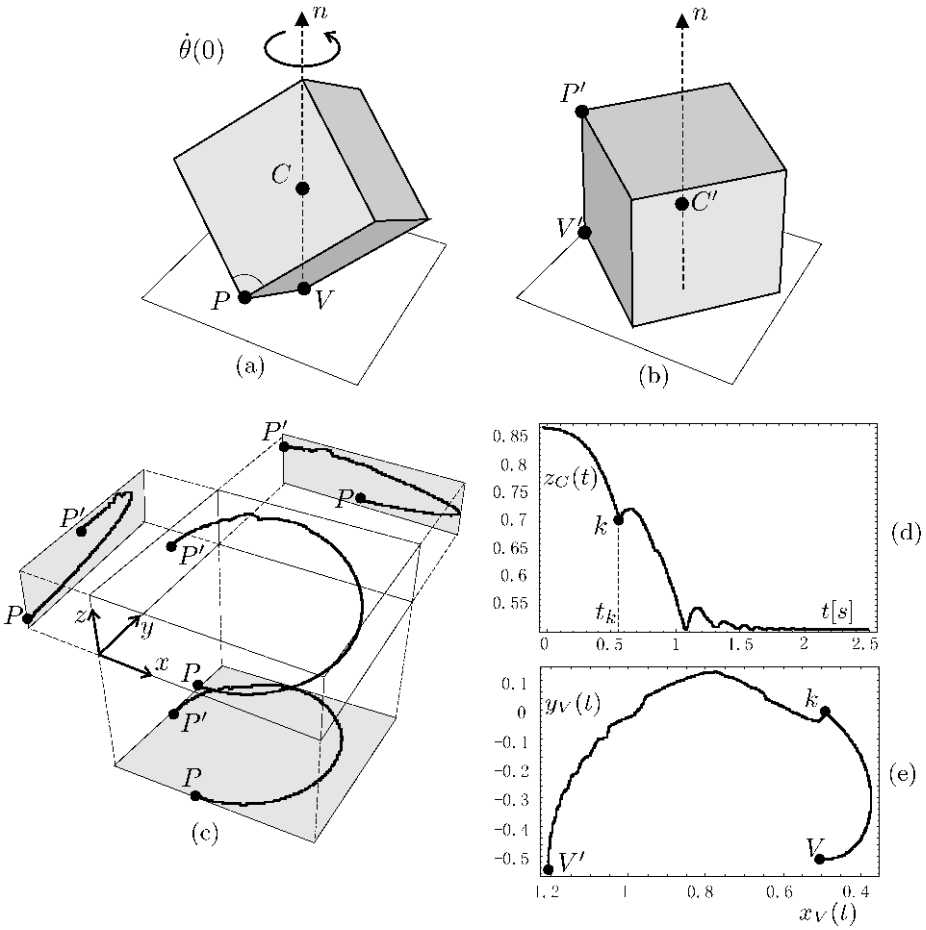

Figure 17. Contact without friction; low initial spin: (a) initial configuration; (b) final configuration; (c) projections on the coordinate planes of the corner P trajectory; (d) C center time-history; (e) V corner trajectory on the x-y plane ($\dot{\theta}(0) = 5\,\mathrm{rad/s}$, $d_0 = 0.002$, $\nu_r = 8$, $\nu_d = 0$, $\nu_f = 0$, $\beta_d = 1000$, $\beta_f = 100$)

first corner. The body is set in motion by assigning, as an initial condition, a spin with axis n and two different values of the angular velocity.

Motions described in Figure 17 (low initial spin) and in Figure 18 (high initial spin) are damped only by a slight dissipation obtained by making the exponents ν_d and ν_f vanish in expressions (20) and (21). In this way the dissipative tractions, originally named friction and impact damping, turn into a dissipative traction on the whole boundary dependent on the velocity but independent of the distance from the support. Each figure is composed of five panels to give an effective description of such complex 3D motions. The top of the figure contains the initial configuration (a) and the final configuration (b). The corner P trajectory and its projections onto coordinate planes are shown in (c).

As can be seen in Figure 17c, corner P performs almost a complete loop. The impact and the following rebound can be observed in Figure 17d at the point marked by k on the graph of the time evolution of the distance of the center C from the

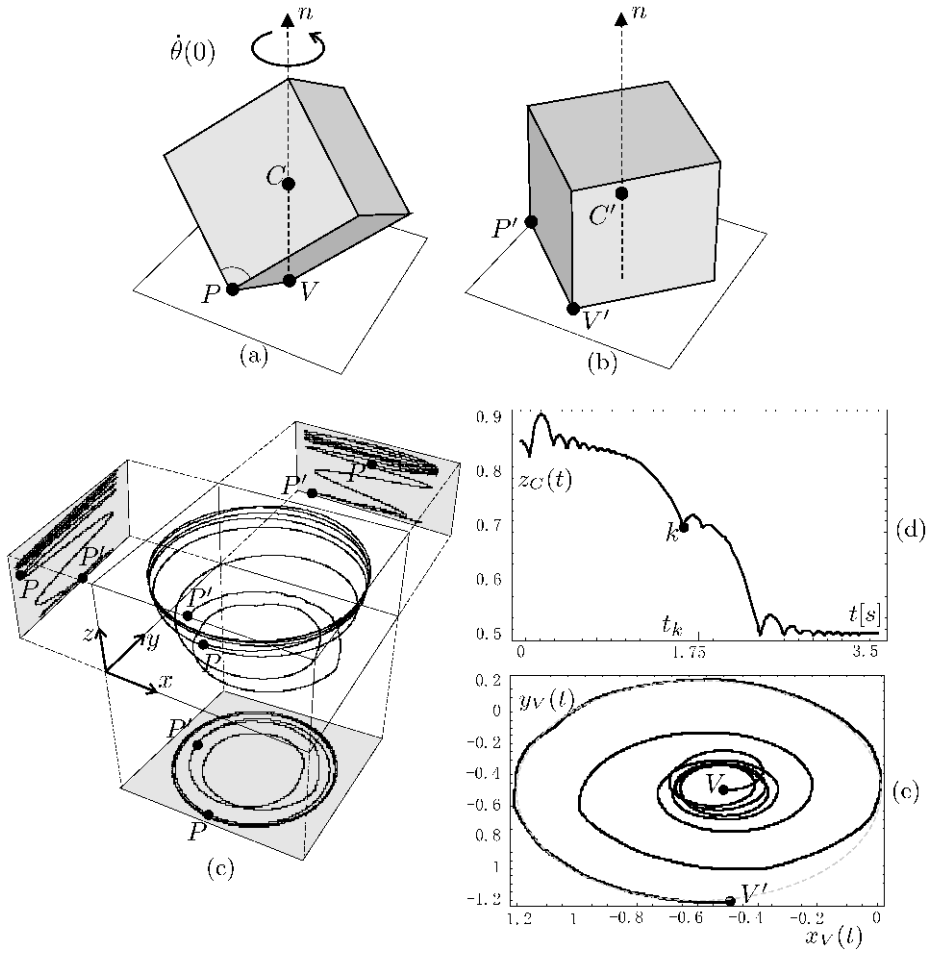

Figure 18. Contact without friction; high initial spin: (a) initial configuration; (b) final configuration; (c) projections on the coordinate planes of the P corner trajectory; (d) C center time-history; (e) V corner trajectory on the x-y plane ($\dot{\theta}(0) = 50\,\mathrm{rad/s}$, $d_0 = 0.002$, $\nu_r = 8$, $\nu_d = 0$, $\nu_f = 0$, $\beta_d = 1000$, $\beta_f = 100$)

support. The same k is used to mark the same event on the V corner trajectory, shown in Figure 17e. It is worth noting that after the rebound the body keeps on rotating for a long time because there is no friction. At last, the P corner reaches a position at a higher level than the initial one while the body ends up sliding on the opposite face containing V. Moreover, it should be noted that neglecting the friction results in the center following a perfectly vertical trajectory.

Figure 18 shows a motion triggered by a spin with the same axis but a higher angular velocity than in the previous case. Again, there is neither friction nor impact damping. In this case point P performs many complete loops. The P corner's persistence on an almost closed trajectory means that the body is moving close to a stable orbit. As the angular velocity decreases, because of the small dissipation, the body slowly moves away from that orbit and reaches a stable equilibrium configuration lying flat on a face. An impact and the following rebound can be observed during this

motion at the point marked by k in Figure 18d. Again, after the rebound, the V corner describes a circular trajectory, as in Figure 18e (the dashed circle).

Friction and impact damping are not neglected any more in the simulations described in Figures 19 and 20. The motion is triggered by a spin with the same axis as before and two different values of the angular velocity. Let us consider the motion in Figure 19 (lower spin). This time the P corner performs about half a loop while an impact and the following rebound occur again at the point marked by k in Figure 19d. After this first impact the angular velocity decreases rapidly because of the friction. As can be observed in the P corner trajectory in Figure 19c, after the impact at k the trajectory becomes quite a straight line since the angular velocity has almost vanished. It is interesting to note how the trajectory of the V corner around which the motion has started, as shown in Figure 19e (black line), is very different from that obtained without friction forces (grey line). In particular, the corner V moves very little further after the impact. Also in this case, the P corner reaches a final position at a higher level than the initial position. The same initial conditions as in the simulation in Figure 18 (higher angular velocity) give rise to the motion described in Figure 20 where both the friction and impact damping have been taken into account. The higher initial angular velocity allows the body to get close to a stable orbit although the number of loops of the P corner trajectory is smaller than in Figure 18. After the impact marked by k in Figure 20d, the angular velocity decreases rapidly because of the friction.

As can be observed in Figure 20c, the P corner trajectory after the impact shows a sharp bent and turns into an almost straight line while the body moves toward a stable equilibrium configuration lying flat on a face. It is worth noting that the P corner trajectory, shown in Figure 20e (black line), is very different from that in the frictionless case (grey line). Again, the V corner moves just a little further after the impact. The trajectories of the body center are not vertical any more because of the friction.

As has been already observed about the 2D simulations, the friction makes the first heavy impact happen later, as can be seen comparing the times t_k in Figure 19d and Figure 20d with those in Figure 17d and Figure 18d.

7.2. Dice throwing

Figures 21 and 22 show other trajectories of a rigid body starting from a configuration close to an unstable equilibrium configuration, with initial vertical displacement $v(0)$, horizontal velocity $\dot{\theta}(0)$ and angular velocity $\dot{\theta}(0)$. The initial spin in Figure 21 has a horizontal axis r while in Figure 22 the spin has the same vertical axis n as in the simulations in Figures 17–20. In both simulations the friction and impact damping have been taken into account, as it can be seen from the graphs of the vertical displacements of C centers in both Figures 21b and 22b, where the motion ends soon after the first rebound. In order to better understand the motion the time-histories of the rotation amplitudes $\theta_2(t)$ and $\theta_3(t)$ have been included as well.

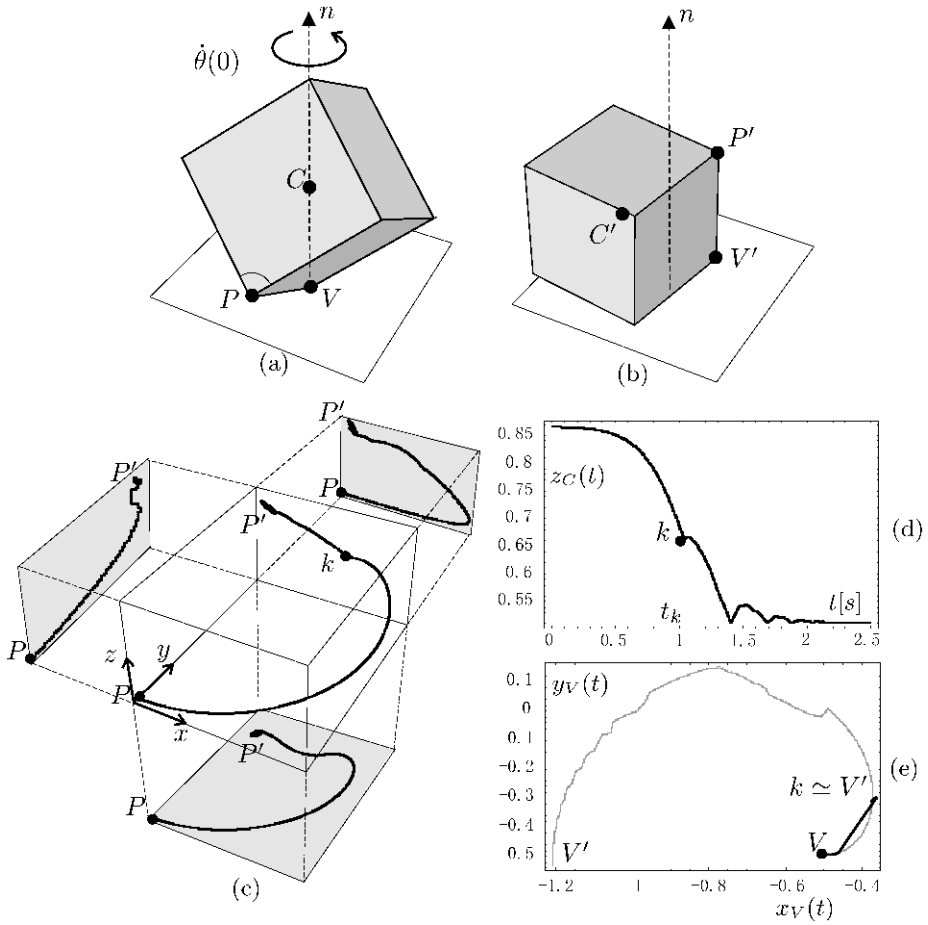

Figure 19. Contact with friction; low initial spin: (a) initial configuration; (b) final configuration; (c) projections on the coordinate planes of the P corner trajectory; (d) C center time-history; (e) V corner trajectory on the x-y plane ($\dot{\theta}(0) = 5\,\mathrm{rad/s}$, $d_0 = 0.002$, $\nu_r = 8$, $\nu_d = 2$, $\nu_f = 2$, $\beta_d = 1000$, $\beta_f = 100$)

7.3. Numerical solving strategy

Using the *MathLink* interface [41], it is possible to delegate specific calculations from within *Mathematica*® to an external program written in a lower-level language, such as C or C++. In this manner, simple, yet computationally demanding numerical computations, such as tight inner loops or function evaluations can be freed from the overhead associated with symbolic computation. The *MathLink* interface in client configuration provides support for connecting to and communication between the external program and the *Mathematica*® kernel. We have used C++ as the language of choice because of its flexibility, portability, and high numerical performance. The external program defines a set of functions which can then be called from within *Mathematica*® and a message-loop which awaits and processes the requests from the *Mathematica*® kernel. Local (where *Mathematica*® is run on the same machine as the external program) and remote (where the external program executes on another machine) connections are possible. The attempt to delegate simple function

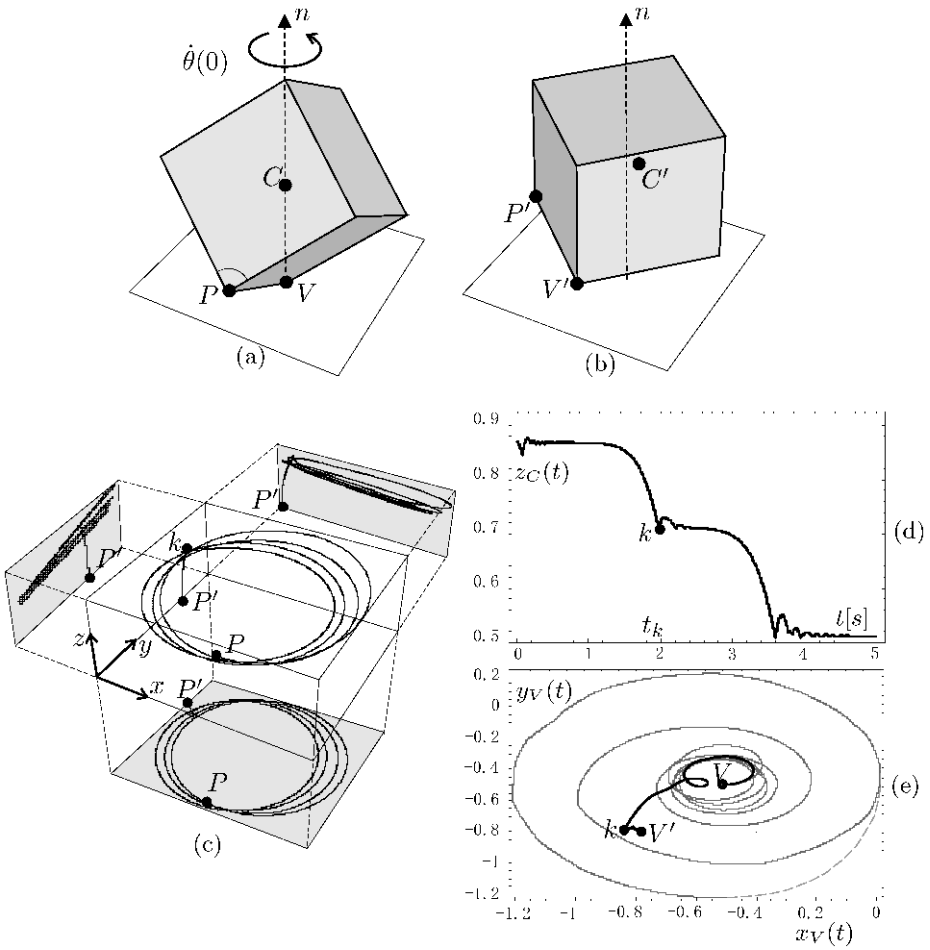

Figure 20. Contact with friction; high initial spin: (a) initial configuration; (b) final configuration; (c) projections on the coordinate planes of the P corner trajectory; (d) C center time-history; (e) V corner trajectory on the x-y plane ($\dot{\theta}(0) = 50\,\mathrm{rad/s}$, $d_0 = 0.002$, $\nu_r = 8$, $\nu_d = 2$, $\nu_f = 2$, $\beta_d = 1000$, $\beta_f = 100$)

evaluations, *i.e.* computations of force densities defined by expressions (19)–(22) to the external C++ program has not improved computation times, because the work-grain size was too small – that is, the overhead of communication between *Mathematica*® and the C++ program dwarfed the actual computation time (which was measured to be in the order of tens of μs for each function evaluation).

The necessity to use larger grains being evident, we have decided to transfer the whole surface integration to the external program, *i.e.*, to calculate the integrals of forces and moments acting on different faces of the rigid body in the shape of a cube, given by Equations (8) and (9), inside the C++ program. A simple and efficient Gaussian 2D integration routine [42] has been used. In this way the grain size has increased by a factor of thousands, making the communication overhead negligible. The overall time gain is impressive – a typical 3D calculation now takes 30 minutes, with only about 10% spent in the *Mathematica*® environment, compared

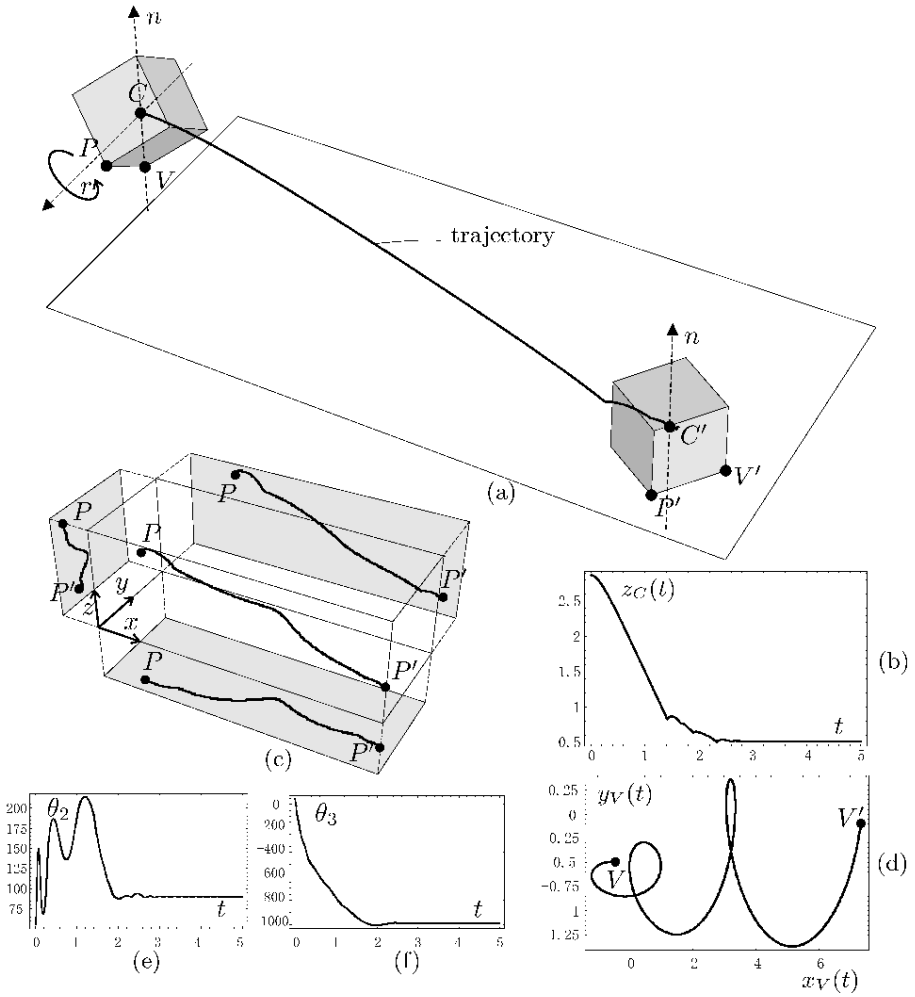

Figure 21. Contact with friction; high initial spin: (a) initial configuration; (b) final configuration; (c) projections on the coordinate planes of the P corner trajectory; (d) C center time-history; (e) V corner trajectory on the x-y plane ($\dot{\theta}(0) = 50\,\mathrm{rad/s}$, $d_0 = 0.002$, $\nu_r = 8$, $\nu_d = 2$, $\nu_f = 2$, $\beta_d = 1000$, $\beta_f = 100$)

to 100 minutes before externalization of the surface integration. In the future, we envision parallelization of the integration routine with the aid of the Message Passing Interface to further reduce the computation times. The integration over time is still achieved by the built-in functions of *Mathematica*® because the potential gain of externalizing this too is small (considering that 85% of time is already spent in the C++ program).

8. Elastic bouncing and vibrations

For plane deformations it is convenient to replace the incompressibility condition by an explicit characterization of the stretch $\boldsymbol{U}$ defined by the polar decomposition:

$$\boldsymbol{F} = \boldsymbol{R}\boldsymbol{U}\,, \tag{23}$$

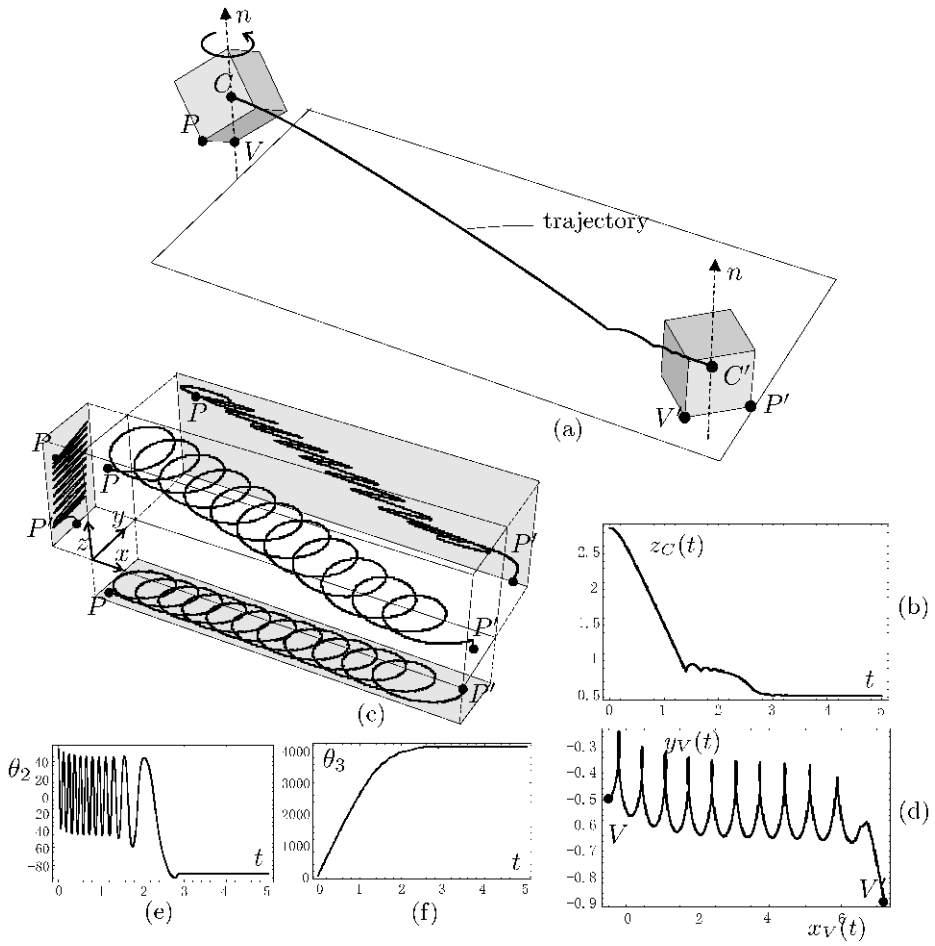

Figure 22. Contact with friction; high initial spin: (a) initial configuration; (b) final configuration; (c) projections on the coordinate planes of P corner trajectory; (d) C center time-history; (e) V corner trajectory on the plane $x-y$ ($\dot{\theta}(0)=50\,\mathrm{rad/s}$, $d_0=0.002$, $\nu_r=8$, $\nu_d=2$, $\nu_f=2$, $\beta_d=1000$, $\beta_f=100$)

where $\boldsymbol{R}$ is a rotation and $\boldsymbol{U}$ is a positive definite tensor. To enforce the incompressibility constraint it is sufficient to parameterize the set of all admissible stretches by giving the matrix of $\boldsymbol{U}$ the following form:

$$\begin{pmatrix} \frac{1+\kappa^2}{\chi} & \kappa & 0 \\ \kappa & \chi & 0 \\ 0 & 0 & 1 \end{pmatrix}, \tag{24}$$

thus getting $\det \boldsymbol{F} = (\det \boldsymbol{R})(\det \boldsymbol{U}) = 1$. The principal stretches are $\{1/\lambda, \lambda, 1\}$ with:

$$\lambda := \frac{1+\kappa^2+\chi^2+\sqrt{(1+\kappa^2)^2+2(\kappa^2-1)\chi^2+\chi^4}}{2\chi}.$$

As has already been done for rigid bodies, also for elastic bodies, a few simple simulations will be used to show the main properties of the contact interaction. Figure 23 shows a cylinder bouncing in a vertical plane motion. Both the friction and impact damping have been neglected. For this reason the time-histories have

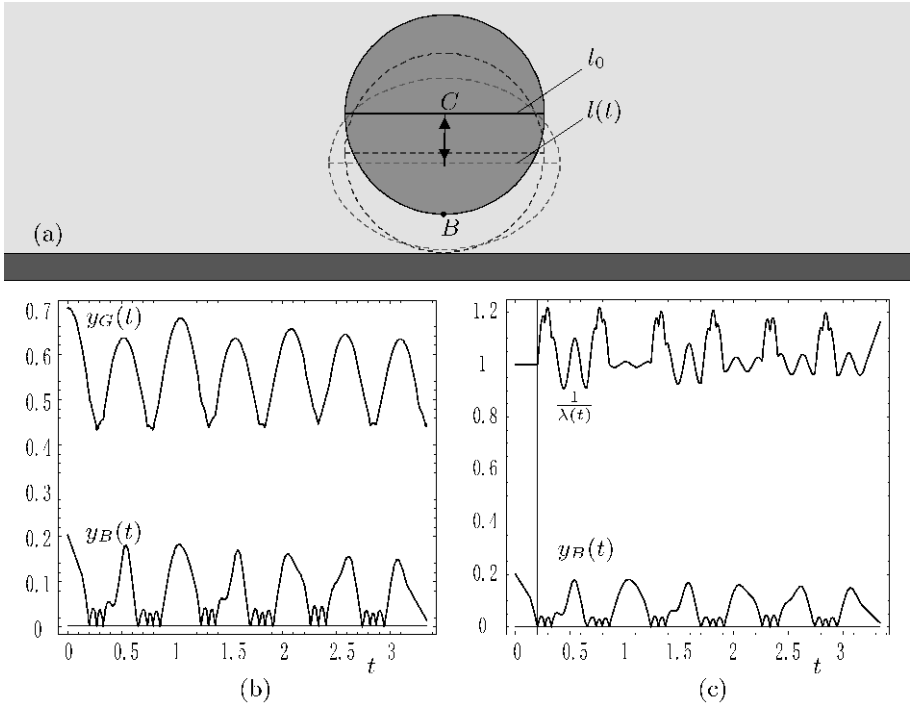

Figure 23. Motion of an elastic cylinder ($d_0 = 0.002\,\mathrm{m}$, $c_{10} + c_{01} = 6 \cdot 10^4$, $\rho = 4 \cdot 10^3\,\mathrm{kg/m^2}$, $\nu_r = 8$, $\nu_d = 2$, $\nu_f = 2$, $\beta_d = 0$, $\beta_f = 10^9\,\alpha_r$, $\mu = 10^2$)

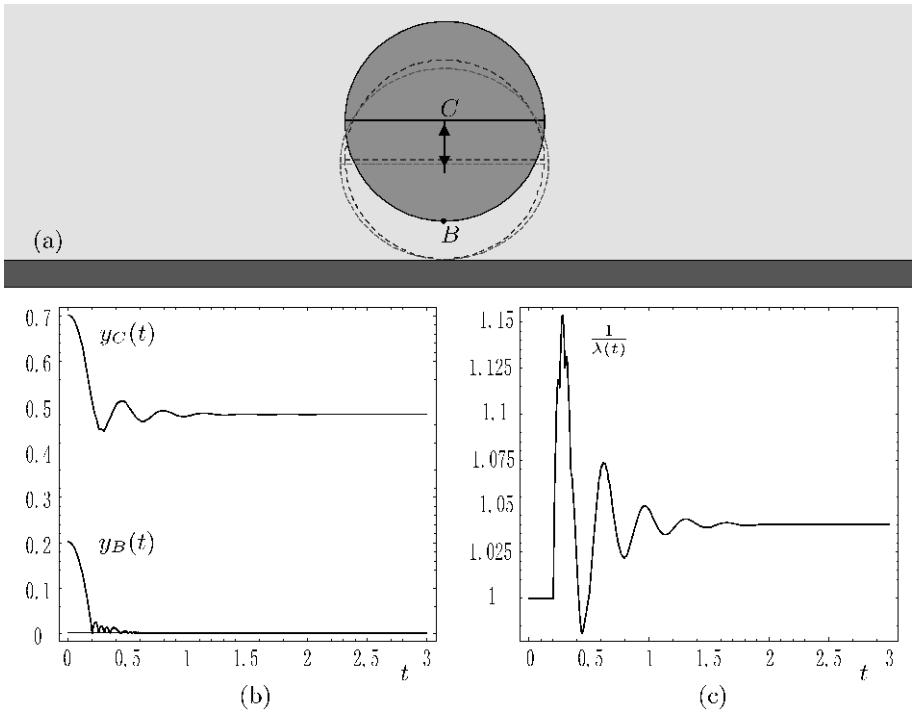

Figure 24. Motion of an elastic cylinder ($d_0 = 0.002\,\mathrm{m}$, $c_{10} + c_{01} = 6 \cdot 10^4$, $\rho = 4 \cdot 10^3\,\mathrm{kg/m^2}$, $\nu_r = 8$, $\nu_d = 2$, $\nu_f = 2$, $\beta_d = 0$, $\beta_f = 10^9\,\alpha_r$, $\mu = 5 \cdot 10^3$)

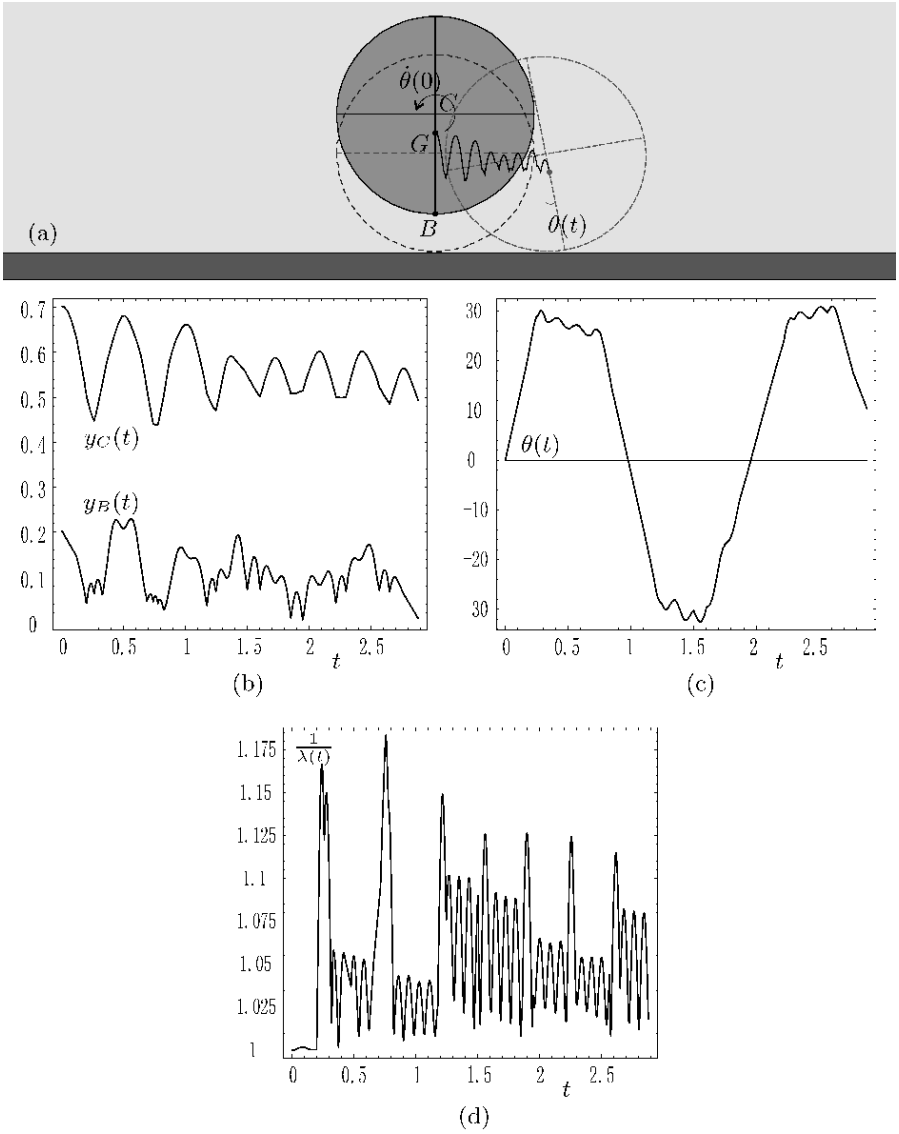

Figure 25. Motion of an elastic cylinder ($d_0 = 0.002\,\mathrm{m}$, $c_{10} + c_{01} = 6 \cdot 10^4$, $\rho = 4 \cdot 10^3\,\mathrm{kg/m^2}$, $\nu_r = 8$, $\nu_d = 2$, $\nu_f = 2$, $\beta_d = 0$, $\beta_f = 0$, $\mu = 10^2$)

been cut before the end of the motion, which is only slightly damped through a low coefficient for the dissipative stress. It is worth noticing how the deformation of the body due to the first impact modifies the bouncing. Comparing the time-histories of the center C and of the contact point B (Figure 23b), we can see a sequence of bounces, due to the motion of the center, together with other bounces with a lower amplitude and a higher frequency, due to the stretching. The frequencies of the two kinds of bouncing seem to be far enough not significantly interacting with each other. In Figure 23c the displacement of the contact point B is related to the time-history of the stretch λ. In this case, since there is only a vertical motion, the stretch is given by the ratio $l(t)/l_0$.

Figure 24 shows the effects of a higher dissipative stress coefficient μ, to be compared with the previous case. After about half a second the dissipation is able to stop the motion. As expected, a higher dissipative stress affects the values of the principal stretches lowering their maximum value, as emerges by comparing the graphs in Figure 23c and Figure 24c.

The body in Figure 25 has a non uniform mass density. The resulting center of mass for a section is not located at the center any more but it is shifted downward in G in the starting configuration. A vertical displacement and an angular velocity have been given as initial conditions. It can be noticed how the rotation time-history (Figure 25c) reflects the change of the contact point.

9. Conclusions

A constitutive approach has been followed in this paper to model the contact between a stiff or soft body and a rigid flat support. The contact is interpreted as an interaction between the body boundary and the support surface modeled by four short range force fields describing: repulsion, adhesion, impact damping and friction. All these short range forces depend on the distance between the body boundary and the support surface. The main advantage of this approach is the ability to describe the motion of a body smoothly during all the different phases of the motion (*i.e.* sliding, rocking, slide-rocking, free flight) by a single set of equations of motion. Furthermore, the same contact force fields can follow the deformable boundary of an elastic body. Just by replacing the rigid body with an affine body model, very realistic motions can be described by numerical simulations even for large deformations, showing the coupling between bouncing and stretching vibrations. A very accurate algorithm is needed to perform the numerical simulations described in the previous sections. A procedure connecting the *Mathematica*® kernel to external C++ programs has proven invaluable in simulating complex 3D motions in a reasonable time on a single processor computer. We plan to improve the computational efficiency by extending this procedure to a multiprocessor system. Movies of the simulations described in this paper can be found in [43].

Acknowledgements

A. Contento acknowledges the support received at the Department of Technical Physics and Applied Mathematics, Gdansk University of Technology, Poland, where he spent a 5-month grant working with J. Dziedzic, in partial fulfillment of his doctoral thesis.

References

[1] Hertz H 1882 *J. Reine Angew. Math.* **92** 156
[2] Johnson K L 1885 *Contact Mechanics*, Cambridge University Press, Cambridge
[3] Wriggers P 2002 *Computational Contact Mechanics*, John Wiley & Sons
[4] Derjaguin B V 1934 *Kolloid Z.* **62** 155
[5] Johnson K L, Kendall K and Robert A D 1971 *Proc. Royal Society London A* **324** 301
[6] Derjaguin B V, Muller V M and Toporob Y P 1975 *J. Colloid and Interface Science* **53** 314
[7] Maugis D 1992 *J. Colloid and Interface Science* **150** 243
[8] Muller V M, Yushchenko V S and Derjaguin B V 1980 *J. Colloid and Interface Science* **77** 91
[9] Attard P and Parker J L 1992 *Phys. Rev. A* **46** 7959

[10] Greenwood J A 1997 *Proc. Royal Society London A* **453** 1277
[11] Feng J Q 2000 *Colloids and Surfaces A: Physicochemical and Engineering Aspects* **172** 175
[12] Wu J J 2006 *Int. J. Solids and Structures* **43** (6) 1624
[13] Wu J J 2006 *J. Physics D: Applied Physics* **39** 351
[14] Argento C, Jagota A and Carter W C 1997 *J. Mech. Phys. of Solids* **45** 1161
[15] Shenton H W and Jones N P 1991 *J. Engng Mech.* **117** (8) 2286
[16] Allen R H, Oppenheim I J, Parker A R and Bielak J 1986 *Earthquake Engineering and Structural Dynamics* **14** 861
[17] Psycharis I N 1990 *Earthquake Engineering and Structural Dynamics* **19** 555
[18] Lödtstedt P 1981 *ZAMM* **61** 605
[19] Lödtstedt P 1982 *SIAM J. Appl. Math.* **42** (2) 281
[20] Panagiotopoulos P D 1993 *Hemivariational Inequalities. Applications in Mechanics and Engineering*, Springer, New York
[21] Pfeiffer F and Glocker C 1996 *Multibody Dynamics with unilateral Constraints*, Wiley, New York
[22] Sinopoli A 1997 *Nonlinear Dynamics* **12** 343
[23] Simo J C, Wriggers P and Taylor R L 1985 *Computer Methods in Applied Mechanics and Engineering* **51** 163
[24] Gallego F J and Anza J J 1989 *International Journal for Numerical Methods in Engineering* **28** 1249
[25] Curnier A and Alart P 1988 *Journal de Mecanique Theorique et Appliquee* **7** 67
[26] Kim NH,Park Y H and Choi K K 2001 *Structural and Multidisciplinary Optimization* **21** 196
[27] Wriggers P and Zavarise G 2004 *Computational Contact Mechanics* Chapter 6, (Stein E, de Borst R, Hughes T J R, Eds) Encyclopedia of Computational Mechanics, John Wiley & Sons, Ltd.
[28] Laursen T A and Simo J C 1993 *Int. J. Num. Meth. in Engng* **36** (20) 3451
[29] Wohlmuth B I 2000 *Discretization Methods and Iterative Solvers based on Domain Decomposition*, Springer, New York
[30] Ciavarella M and Barber J R 2005 *European Journal of Mechanics A/Solids* **24** 371
[31] Cattaneo C 1938 *Rendiconti dell'Accademia Nazionale dei Lincei* **27** 342 , 434, 474
[32] Mindlin R D 1949 *J. Appl. Mech.* **16** 259
[33] Ciavarella M 1998 *Int. J. Solids and Structures* **35** 2349
[34] Jäger J 1998 *J. Tribology* **120** 677
[35] Wriggers P, Vu Van T and Stein E 1990 *Computers and Structures* **37** 319
[36] Archard J F 1957 *Proc. Royal Society London A* **243** 190
[37] Greenwood J A and Williamson J B P 1966 *Proc. Royal Society London A* **295** 300
[38] Majumdar A and Bhushan B 1990 *J. Tribology* **112** 205
[39] Carpinteri A, Chiaia B and Invernizzi S 1999 *Theoretical and Applied Fracture Mechanics* **31** 163
[40] Borri-Brunetto M, Carpinteri A and Chiaia B 1998 *Lacunarity of the Contact Domain between Elastic Bodies with Rough Boundaries* Probabilities and Materials. Tests, Models and Applications, NATO ASI Series 3, Kluwer Academic Publishers, Dordrecht
[41] *http://www.wolfram.com/solutions/mathlink/mathlink.html*
[42] Kułak L private communication
[43] *http://ing.univaq.it/tatone/projects/contact/contact.php*